Size-dependent evolution of the atomic vibrational density of states and thermodynamic properties of isolated Fe nanoparticles

B. Roldan Cuenya,[1,*] L. K. Ono,[1] J. R. Croy,[1] K. Paredis,[1] A. Kara,[1] H. Heinrich,[1] J. Zhao,[2] E. E. Alp,[2] A. T. DelaRiva,[3] A. Datye,[3] E. A. Stach,[4] and W. Keune[5,6]

[1]*Department of Physics, University of Central Florida, Orlando, Florida 32826, USA*

[2]*Advanced Photon Source, Argonne National Laboratory, Argonne, Illinois 60439, USA*

[3]*Department of Chemical and Nuclear Engineering, University of New Mexico, Albuquerque, New Mexico 87131, USA*

[4]*Center for Functional Nanomaterials, Brookhaven National Laboratory, Upton, New York 11973*

[5]*Max Planck Institute of Microstructure Physics, Weinberg 2, 06120 Halle, Germany*

[6]*Department of Physics, University of Duisburg-Essen, 47048 Duisburg, Germany*

(Received 31 March 2012; published 2 October 2012)

We have gained insight into the internal degree of atomic disorder in isolated size-selected Fe nanoparticles (NPs) (∼2–6 nm in size) supported on SiO_2/Si(111) and Al_2O_3(0001) from precise measurements of the low-energy (low-E) part of the phonon density of states [PDOS, $g(E)$] via ^{57}Fe nuclear resonant inelastic x-ray scattering (NRIXS) combined with transmission electron microscopy (TEM) measurements. An intriguing size-dependent trend was observed, namely, an increase of the low-E excess density of phonon states (as compared to the PDOS of bulk bcc Fe) with increasing NP size. This is unexpected, since usually the enhancement of the density of low-E phonon modes is attributed to low-coordinated atoms at the NP surface, whose relative content increases with decreasing NP size due to the increase in the surface-to-volume ratio. Our NPs are covered by a Ti-coating layer, which essentially restores the local neighborhood of surface Fe atoms towards bulk-like coordination, reducing the surface effect. Our data can be qualitatively explained by the existence of low-coordinated Fe atoms located at grain boundaries or other defects with structural disorder in the interior of the large NPs (∼3–6 nm), while our small NPs (∼2 nm) are single grain and, therefore, characterized by a higher degree of structural order. This conclusion is corroborated by the observation of Debye behavior at low energy [$g(E) \sim E^n$ with $n \sim 2$] for the small NPs, but non-Debye behavior (with $n \sim 1.4$) for the large NPs. The PDOS was used to determine thermodynamic properties of the Fe NPs. Finally, our results demonstrate that, in combination with TEM, NRIXS is a suitable technique to investigate atomic disorder/defects in NPs. We anticipate that our findings are universal for similar NPs with bcc structure.

DOI: 10.1103/PhysRevB.86.165406 PACS number(s): 63.22.Kn, 63.20.D−, 65.80.−g

I. INTRODUCTION

Nanostructured materials have been shown to display unique modifications of their thermodynamic properties as compared to those of the corresponding bulk materials.[1–4] Some examples of thermal quantities that are modified at the nanoscale are lattice specific heat (C_v),[5–8] vibrational entropy (S_{vib}),[2,4,9,10] atomic mean square displacement ($\langle x^2 \rangle$) and Debye temperature (Θ_D),[11–15] thermal expansion,[16,17] melting temperature,[18] and lattice thermal conductivity.[19,20] As the thermodynamic properties originate from the atomic vibrational dynamics, it remains highly desirable to examine in detail the lattice dynamics (i.e., phonons) in nanostructured materials and, in particular, in nanoparticles (NPs).[2,21,22] Thermodynamic properties play a role in the thermal stability and operation regime of nanocatalysts,[23] heat generation and distribution in plasmonic nanoantennas (thermoplasmonics),[24] thermoelectric devices,[25] and the efficiency of nanostructured metal-organic composites in solar cells.[26] In addition, knowledge of the vibrational dynamics is relevant to the understanding of fundamental processes in nanostructures, such as temperature-dependent atomic order–disorder transitions,[27] structural phase transitions involving soft phonon modes,[28,29] and thermally activated phenomena described by the pre-exponential factor[30] in Arrhenius-type processes on the surface of NPs (e.g., diffusion and surface chemical reactions[31]).

The fundamental quantity for the description of the atomic vibrational dynamics in nanostructured materials is the vibrational (or phonon) density of states [PDOS, $g(E)$]. The vibrational properties of nanocrystalline materials (nanocomposites) have been extensively studied theoretically[7,8,10,13,43–47] as well as experimentally by inelastic neutron scattering and nuclear resonant inelastic x-ray scattering (NRIXS).[9,32–42] Nanocrystalline materials are extended systems and have compacted polycrystalline aggregates with grain sizes in the nanometer regime and are dominated by grain boundaries.[48,49] The sensitivity of the PDOS to structural order/disorder was previously demonstrated for Ni_3Al alloys by Fultz *et al.*[32] and nanocrystalline $Fe_{90}Zr_7B_3$ by Stankov *et al.*[50] Clear differences between the PDOS of nanocrystalline and bulk materials have been observed, in particular, an enhancement of $g(E)$ for nanocrystalline materials at low- and high-phonon energies and broadening and damping of the PDOS features. In agreement with numerical simulations,[7,10,13,44–47] NRIXS results have demonstrated that this anomalous enhancement of $g(E)$ originates from the contribution to the PDOS of the interfaces at grain boundaries,[42] although oxidation might also play a role.[9,36,38,39] On the other hand, there is a need for the experimental investigation of the PDOS of isolated nanoscale systems, such as self-assembled size-selected NPs, as such studies are scarce.[51–53] Enhancement of $g(E)$ at low and high E and damping/shift of the phonon peaks were observed in such NPs by NRIXS.[51–53] These findings agree with theoretical

calculations of the PDOS in free-standing (unsupported) isolated NPs[3,4,7,8,11,12,54–56] and in supported isolated NPs on a Ag substrate.[51] The excess modes at high E were attributed to atomic vibrations in a hard subsurface transition shell[3,4] or to compressive stress[7,51,54] in isolated NPs. The low-E enhancement is attributed to vibrations of undercoordinated atoms at the surface of NPs.[3,4,7,11,12,30,51,55,57] Nevertheless, the physical nature of the low-E excess modes in nanostructured systems is a matter of current debate as linear,[3,37,47,55] nonlinear,[7,45,46,51,58] and Debye-like quadratic[9,32–34,36,38,40,44] behaviors of $g(E)$ have been reported.

In this context, in the present work we investigate the size dependence of the PDOS of supported, isolated, size-selected ^{57}Fe NPs by NRIXS. Contrary to isolated ^{57}Fe NPs reported earlier,[51] the NPs here have been capped by a Ti layer, which prevents NP oxidation. In addition, the titanium coating results in the suppression of surface effects due to the restoration of the atomic coordination. We focused our study on the low-E excess vibrational modes in order to extract their power-law [$g(E) \sim E^n$] behavior and gain insight into their origin. Furthermore, from the measured $g(E)$ we were able to determine important thermodynamic quantities of the NPs, which are compared to those of bulk bcc Fe.

II. EXPERIMENTAL

Size-selected ^{57}Fe NPs were synthesized via inverse micelle encapsulation.[52,53,59] Nonpolar/polar diblock copolymers [PS(x)-P2VP(y)] were dissolved in toluene (nonpolar) to form reverse micelles and subsequently loaded with a $^{57}FeCl_3$ salt. The NP size was tuned by using polymers with different head sizes (P2VP) and by changing the metal salt to P2VP ratio. The interparticle distance was modified by selecting polymers with different tail lengths (PS). A monolayer-thick film of ^{57}Fe NPs was obtained upon dip-coating Al_2O_3(0001) (sample S1) and SiO_2(4 nm)/Si(111) (samples S2–S6) substrates into the metal-loaded polymeric solution.[50]

The *ex situ* prepared samples were transferred into an ultrahigh vacuum (UHV) system (SPECS GmbH) for additional *in situ* preparation and chemical characterization. The encapsulating polymer was removed in UHV via an O_2-plasma treatment ($P[O_2] = 4.0 \times 10^{-5}$ mbar for 100 min) at room temperature (RT). X-ray photoelectron spectroscopy (XPS) measurements revealed the removal of the organic ligands as well as other possible residues from the *ex situ* NP synthesis, since no C-1s (285.2 eV) and Cl-2s (270.0 eV) signals were detected. Subsequently, the oxidized ^{57}Fe NPs were subjected to a H_2-plasma treatment ($P[H_2] = 1.0 \times 10^{-4}$ mbar for 120 min) at 600 °C. After this treatment, the reduction of the NPs was confirmed by XPS. Finally, the samples were coated by 5 nm of titanium at RT via physical vapor deposition (UHV) in order to prevent the oxidation of the metallic ^{57}Fe NPs during the *ex situ* NRIXS measurements. Six samples with different NP sizes (labeled S1–S6) were prepared and investigated. Additional details on the sample preparation parameters are included in Table I and the Supplemental Material,[60] Figs. 1 and 2.

Morphological characterization of the ^{57}Fe NP samples supported on single crystals was carried out via atomic force microscopy (AFM) and cross-sectional transmission electron microscopy (TEM, Tecnai 300 kV, University of Central Florida). The TEM cross sections were prepared with a focused ion beam system (FIB, FEI 200). In addition, ^{57}Fe NP samples

TABLE I. Summary of the parameters used for the synthesis of size-selected ^{57}Fe NPs supported on Al_2O_3(0001) (S1) and SiO_2/Si(111) (S2–S6). The NP heights and interparticle distances obtained from the analysis of AFM images taken at RT after polymer removal by an O_2-plasma treatment and subsequent NP reduction by an H_2-plasma treatment at 600 °C are also shown.

Sample	PS/P2VP molecular weight (g/mol)	$^{57}FeCl_3$/P2VP ratio	Particle height (nm)	Interparticle distance (nm)
S1	16000/3500	0.4	2.1 (0.9)	32(5)
S2	16000/3500	0.4	1.8 (0.5)	36(5)
S3	27700/4300	0.6	2.4 (0.7)	33(4)
S4	27700/4300	0.2	3.1 (1.1)	42(4)
				67(9)
S5	53400/8800	0.6	4.0 (1.3)	47(8)
S6	48500/70000	0.1	5.9 (2.1)	60(10)

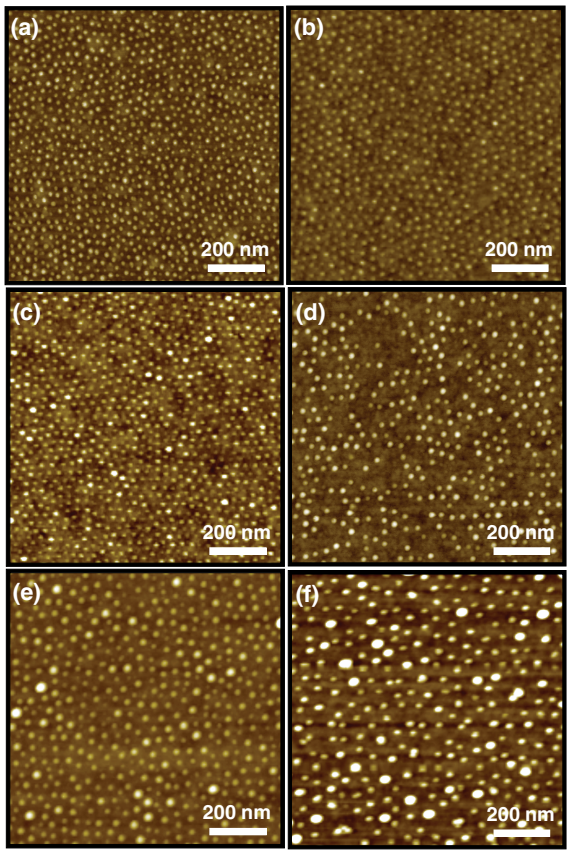

FIG. 1. (Color online) 1×1 μm^2 tapping mode AFM images of H_2-plasma treated ^{57}Fe NPs supported on Al_2O_3(0001) (sample S1) and SiO_2/Si(111) (samples S2–S6) synthesized by inverse micelle encapsulation using diblock copolymers with different head and tail lengths. (a), (b) PS(16000)-P2VP(3500) [S1, S2]; (c), (d) PS(27700)-P2VP(4300) [S3, S4]; (e) PS(53400)-P2VP(8800) [S5]; and (f) PS(48500)-P2PV(70000) [S6].

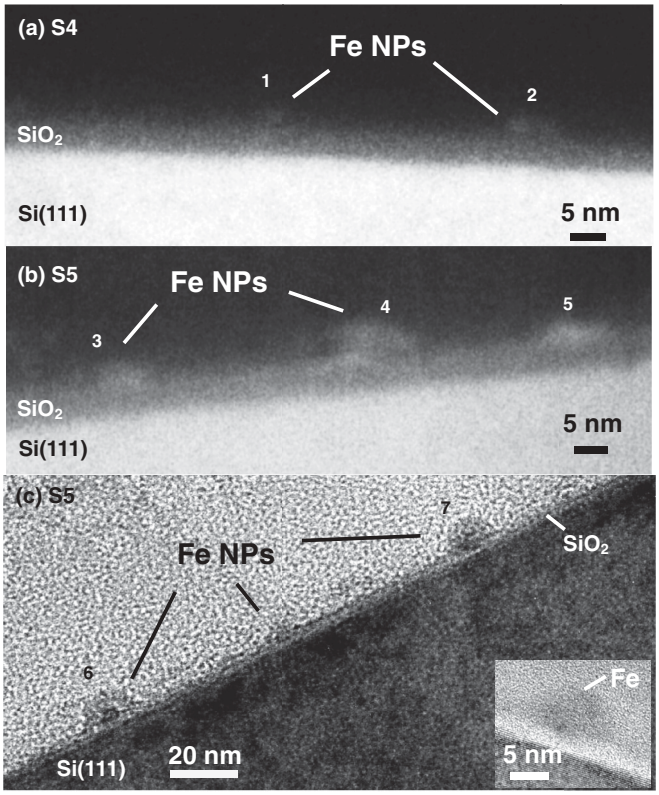

FIG. 2. Cross-sectional TEM images of ^{57}Fe NPs in (a) sample S4 and (b), (c) sample S5. Images (a) and (b) represent HAADF scanning transmission electron micrographs, while (c) is a bright field image. The inset in (c) shows an Fe NP in sample S5. The numbers in the images label the observed NPs.

drop coated on SiO_2(20 nm)/Si TEM grids were investigated after an analogous polymer removal treatment in UHV, in order to gain further insight into their crystalline structure, and were imaged at the University of New Mexico using a JEOL 2010F microscope and at Brookhaven Nat. Lab. using a Titan 80–300, Cs-corrected TEM. The aberrations were corrected to a flat phase field of greater than 20 mrad. Exit wave reconstructions were performed using MacTempas, and aberrations were corrected by maximizing the phase range. NRIXS measurements were performed at RT in air at the beamline 3-ID at the Advanced Photon Source (Argonne National Laboratory). The synchrotron beam was scanned (± 80 meV) around the nuclear transition energy of the ^{57}Fe nucleus at 14.413 keV with an energy resolution of 1.3 meV. The measurement time per sample was 1–2 days. The PHOENIX software was used for decomposing the measured spectra into single-phonon and multiphonon contributions.[61] The one-phonon term is proportional to the vibrational density of states, [PDOS, $g(E)$]. The analysis is based on the harmonic approximation of lattice vibrations.[61]

III. RESULTS

A. Morphological, structural, and chemical characterization (AFM, TEM, XPS)

Figure 1 shows AFM images from ^{57}Fe NPs of different sizes deposited on Al_2O_3(0001) (S1) and SiO_2/Si(111) (S2–S6): (a) S1, (b) S2, (c) S3, (d) S4, (e) S5, and (f) S6, acquired after polymer removal and subsequent annealing at 600 °C under an atomic hydrogen environment. The AFM images demonstrate that the NPs are isolated from each other and of nearly uniform size. The average NP heights and interparticle distances extracted from the AFM measurements are included in Table I and the corresponding histograms in the Supplemental Material,[60] Figs. 1 and 2, respectively.

Representative cross-sectional TEM images of ligand-free and uncoated NPs are shown in Fig. 2 for S4 (a) and S5 (b), (c). The images in (a) and (b) correspond to Z-contrast high angle annular dark field (HAADF) measurements, while those in (c) contain bright field data. From the limited set of NPs visualized in these cross-sectional samples (50–100 nm thick), the following TEM NP height (h), diameter (d), and aspect ratio (r) were obtained: (a): (1) $h = 2.5$ nm, $d = 5$ nm, $r = 0.5$; (2) $h = 2.4$ nm, $d = 5.5$ nm, $r = 0.4$ (S4); (b): (3) $h = 3.8$ nm, $d = 6.1$ nm, $r = 0.6$; (4) $h = 4.4$ nm, $d = 10.2$ nm, $r = 0.4$; (5) $h = 3.5$ nm, $d = 9.4$ nm, $r = 0.4$ (S5). The NP sizes estimated from the bright field images of S5 in (c) are (6) $h = 6.2$ nm, $d = 11.4$ nm, $r = 0.5$; and (7) $h = 6.2$ nm, $d = 11.6$ nm, and $r = 0.5$. The inset in Fig. 2(c) displays an Fe NP with $h = 5.8$ nm, $d = 9.6$ nm, and $r = 0.6$. The smaller NPs in samples S1–S3 could not be visualized because of the weak contrast in the images of uncoated samples due to the oxidation of the Fe NPs upon air exposure. The same contrast problem was observed when cross-sectional samples of the Ti-coated NPs (those investigated here via NRIXS) were studied. It should be noted that large error margins in the estimation of the NP sizes in Fig. 2 arise due to their poor contrast. Nevertheless, our images revealed hemispherical NP shapes for all NPs.

In order to better resolve the crystalline structure of our ^{57}Fe NPs, NP solutions were drop coated onto SiO_2/Si TEM grids. These samples were uncoated and exposed to air before the TEM analysis. Therefore, in the TEM measurements, the NP surface is expected to be oxidized. Some typical high resolution TEM images of those samples are shown in Figs. 3 and 4. The average NP diameters (after measuring two perpendicular diameters in order to take into consideration NP asymmetry) in Fig. 3 are (a) $d = 26.2$ nm, (b) $d = 15.4$ nm, (c) 10.2 nm, and in Fig. 4(a) $d = 4.0$ nm and (c) $d = 4.1$ nm. It should be noticed that for hemispherical NPs the NP diameters measured by TEM are double the NP height measured by AFM. In general, the smaller NPs were found to be single crystals [Figs. 4(a) and 4(c)], while internal planar defects (twin boundaries, stacking faults) were observed in the larger particles, see Figs. 3(a)–3(c). The lattice fringes measured for the larger particles are 1.98 Å, which agree within experimental error with the bulk bcc Fe(110) spacing of 2.03 Å. Phase identification requires that the crystal is oriented along its zone axis, yielding a set of noncollinear lattice fringes. However, NPs generally exhibit only a one-dimensional fringe, since the particles are rarely aligned along their zone axis.[62,63] Even after counting only particles that were aligned along their zone axis, Tsen *et al.*[62] found a measurement error of ± 0.5 Å. The observed lattice spacings we report in Fig. 3 are well within experimental error with respect to 2.03 Å of bulk bcc Fe.

Figure 5 displays XPS spectra from the Fe-2p core level region of NPs in S2 after exposure to (i) an O_2-plasma

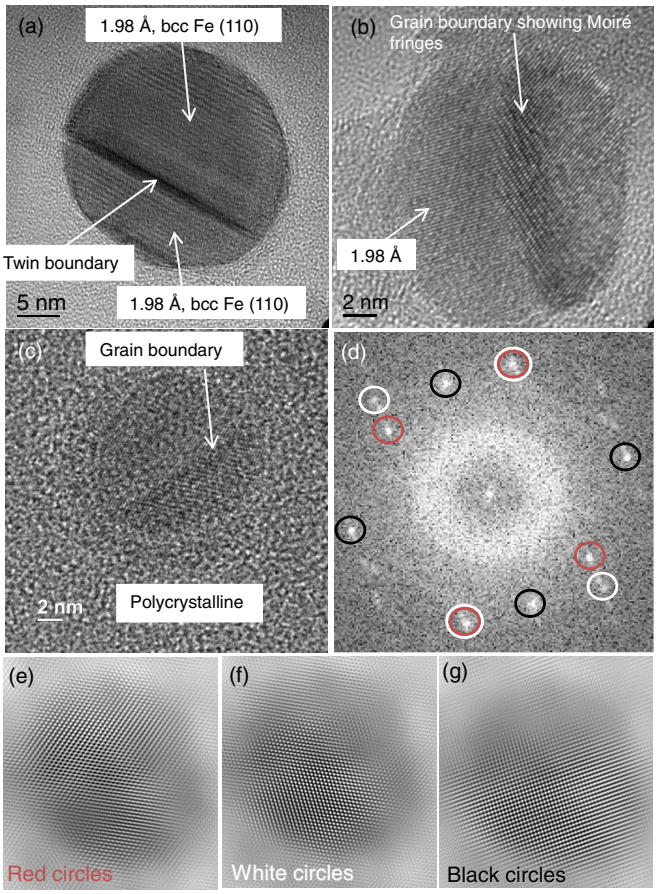

FIG. 3. (Color online) High resolution TEM images of ^{57}Fe NPs deposited onto SiO_2(20 nm)/Si grids. The NP diameters are (a) 26.2 nm, (b) 15.4 nm, and (c) 10.2 nm, respectively. Each of these large NPs shows some form of planar defect (e.g., twin boundary and/or grain boundary). (c) Exit wave reconstruction, showing the modulus squared of the exit wave. Images of this type result in enhanced image resolution (but at the cost of contrast). (d) Fast Fourier Transform (diffractogram) of (c); the images in (e)–(g) are inverse Fast Fourier Transforms based on selectively back transforming the regions (circles) described in (d). (e)–(g) Demonstrates that this large NP is polycrystalline.

treatment at RT, followed by (ii) a H_2-plasma treatment at 600 °C. Only a Fe^{3+} signal ($2p_{3/2}$ in Fe_2O_3 at 711.1 eV)[64] was detected on these samples by XPS after atomic oxygen exposure, indicating that the NPs were completely oxidized [Fig. 5(a)]. The peaks labeled as Fe* correspond to iron-oxide satellite features. After the *in situ* reduction treatment [Fig. 5(b)], the XPS peaks observed correspond to metallic Fe (Fe^0-$2p_{3/2}$ at 707.0 eV).[64] Additional XPS spectra from the rest of the samples (S1, S3–S6) after *in situ* reduction can be found in the Supplemental Material,[60] Fig. 3.

B. Vibrational characterization (NRIXS)

Figure 6(a) shows NRIXS spectra (raw data) from ^{57}Fe NPs supported on Al_2O_3(0001) (S1) and SiO_2/Si(111) (S2–S6) measured at RT. The main features of these spectra are an intense and sharp elastic peak at $E = 0$ meV (Mössbauer or zero-phonon line) and side bands at higher and lower excitation energies E corresponding to phonon-assisted excitation of the

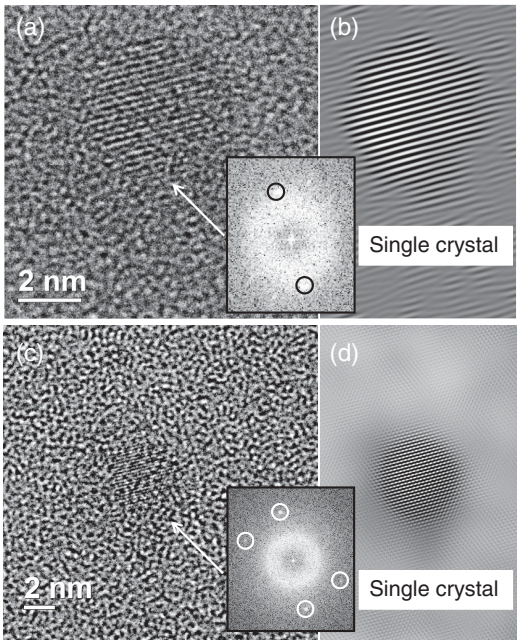

FIG. 4. High resolution TEM images of small ^{57}Fe NPs deposited onto SiO_2(20 nm)/Si grids, with sizes of (a) 4.0 nm and (c) 4.1 nm. The insets show the diffractograms and regions of the diffractograms (circles) selected for the Fourier filtered images on the right (b), (d). These Fourier filtered images clearly indicate that the small particles are single crystalline.

nuclear resonance by photons via phonon creation ($E > 0$) and annihilation ($E < 0$).[65–67]

The Fe-projected PDOS, $g(E)$, of the NP samples and a reference bulk bcc ^{57}Fe foil obtained from NRIXS measurements are shown in Fig. 6(b). Clear differences between $g(E)$ of the NP samples and bulk bcc Fe are observed.

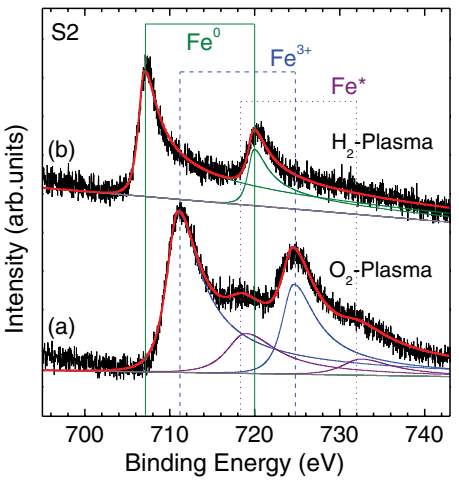

FIG. 5. (Color online) XPS spectra (Al-K$\alpha = 1486.6$ eV) corresponding to the Fe-2p core level of ^{57}Fe NPs deposited on SiO_2/Si(111) (sample S2). The XPS spectra were acquired after polymer removal by an O_2-plasma treatment at RT (a) and after subsequent *in situ* NP reduction via a H_2-plasma treatment at 600 °C (b). The peaks labeled as Fe* in (a) correspond are satellite features typical of iron oxides.

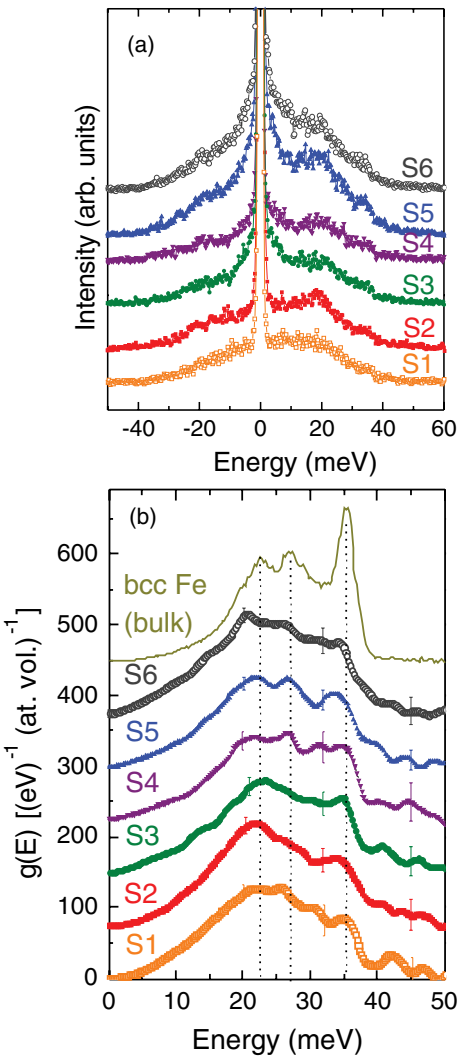

FIG. 6. (Color online) (a) NRIXS spectra from ^{57}Fe NPs supported on $Al_2O_3(0001)$ (sample S1) and $SiO_2/Si(111)$ (samples S2–S6) measured at RT. The spectra are vertically displaced for clarity. (b) PDOS, $g(E)$, obtained from the data is shown in (a). The average NP height in the different samples ranges from ∼2 nm (S1, S2) to ∼6 nm (S6). Also shown is the measured $g(E)$ of bulk bcc ^{57}Fe. The curves in (b) are vertically displaced for clarity by 75 units. Some typical errors are given as vertical bars; below ∼15 meV the errors are within the size of the drawn symbols. The vertical dotted lines indicate the position of the phonon peaks of bulk bcc Fe.

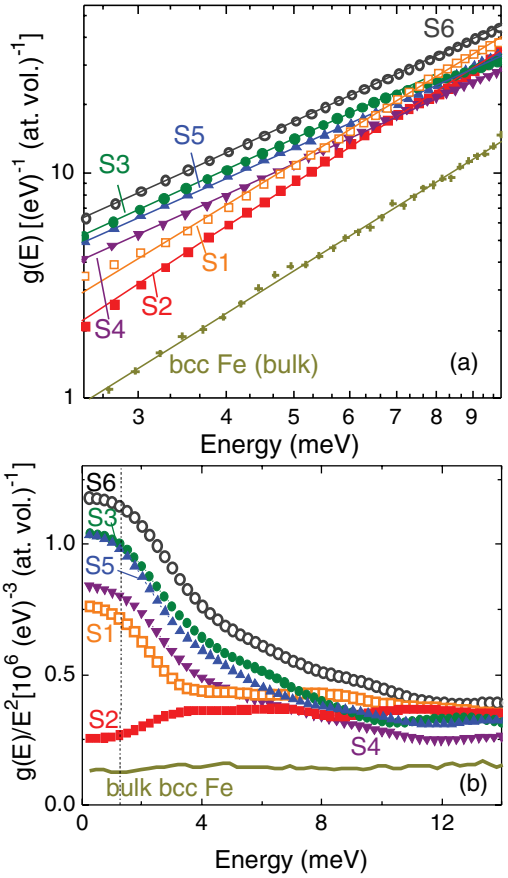

FIG. 7. (Color online) (a) Double-log plot of the low-E region of the PDOS, $g(E)$. The corresponding least-squares fits, $g(E) \sim E^n$, are also shown as full drawn lines. (b) Reduced PDOS, $g(E)/E^2$, versus energy E for ^{57}Fe NP samples (S1–S6) and bulk bcc Fe. The vertical dashed line at $E = 1.3$ meV indicates the energy resolution of the instrumental function.

First, a strong suppression of the LA phonon peak at ∼35 meV is detected for the NPs, an effect that may be attributed to phonon damping due to confinement.[9,44,51,68] In addition, a shift of the LA peak to lower energies (up to 1.3 meV shift for S5) is found. Besides, the transverse acoustic modes near ∼27 meV and ∼22 meV are still clearly observed in some of the NP samples (e.g., S4, ∼3.1 nm; S5, ∼4 nm). Nevertheless, their relative intensities with respect to the ∼35 meV peak are different from those in bulk bcc Fe, with the low phonon features being more prominent in the large NP samples (e.g., S5). Although the experimental error bars are large at high energies, there is a tendency for an enhancement of the PDOS above 40 meV. Here, a high E contribution cannot be assigned to the presence of oxidic Fe species (∼42–43 meV Fe_2O_3 phonon feature)[51] since our *in situ* H_2-plasma treatment led to complete reduction of the NPs [Fig. 5(b)]. Furthermore, the samples were protected by a thin Ti film before air exposure. Although the enhancement of the PDOS at energies above 40 meV might contain interesting physics, the error margin in the present experiment is large in that energy region, which prevents us from drawing definite conclusions. In the following we will focus on the more accurately measured low-E part of $g(E)$.

Figure 7(a) displays a log-log plot of the low-E portion of the PDOS of our ^{57}Fe NPs. Following the Debye model, a $g(E) \sim E^n$ dependence with $n = 2$ is expected in three dimensions (3D) and $n = 1$ in two dimensions (2D). A linear fit of the data displayed in Fig. 7(a) within the energy range of 2.5–10 meV leads to the following n values: $n \approx 1.9$–2.0 (S1 and S2), $n \approx 1.4$ (S3–S6). Surprisingly, only the smallest NPs (S1, S2) investigated closely follow the Debye behavior typical of bulk materials ($n = 1.94$ was obtained for our bulk bcc-Fe foil). The deviations in the behavior of most of our NP samples with respect to the 3D-Debye model at low phonon energies can also be clearly seen in Fig. 7(b). Here the reduced PDOS, $g(E)/E^2$, is shown for our different samples. Considering the

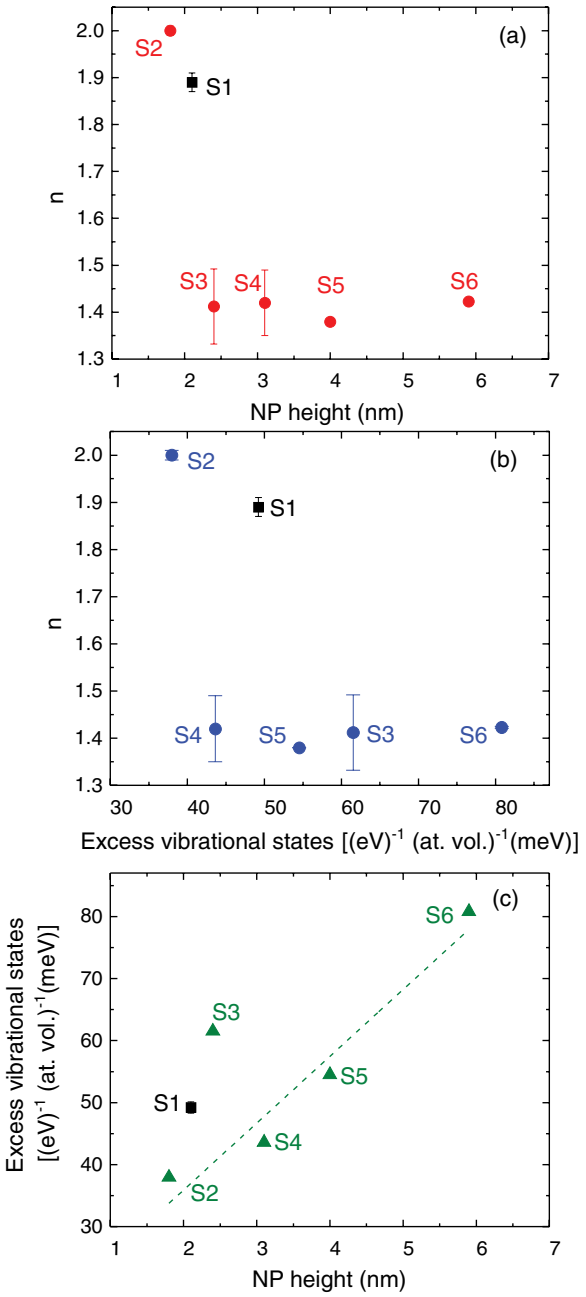

FIG. 8. (Color online) (a) Coefficient n in $g(E) \sim E^n$ displayed versus the NP height for ^{57}Fe NPs (samples S1–S6). (b) Coefficient n versus excess vibrational states (relative to bulk bcc Fe). (c) Excess vibrational states versus the NP height. (The dashed straight line is a guide for the eye.) The substrate is $Al_2O_3(0001)$ for S1 and $SiO_2/Si(111)$ for S2–S6.

1.3 meV resolution, data below 1.3 meV [dashed vertical line in Fig. 7(b)] are physically meaningless in our experiments. A more conservative resolution estimate is a lower limit of twice that value, i.e., 2.6 meV. While samples S1 and S2 (and our bulk bcc Fe reference) follow the 3D-Debye behavior between ~3 meV and 10 meV, S3–S6 reveal a more complex functional behavior in Fig. 7(b), with strong excess PDOS and lattice softening. However, as can be observed in Fig. 7(b), $g(E)/E^2$ values in the linear region of S1 and S2 are also considerably higher than $g(E)/E^2$ for bulk bcc Fe. This trend also demonstrates overall lattice softening of the NPs in S1 and S2 (the smallest NPs) relative to bulk bcc Fe, however, without losing their 3D-Debye characteristics. As the intersection of the extrapolated horizontal constant Debye-like $g(E)/E^2$ function with the vertical axis in Fig. 7(b) is inversely proportional to the cube of the Debye sound velocity,[69] v_D, NPs in S1 and S2 are characterized by a lower average speed of sound than bulk bcc Fe.

Figure 8(a) shows the coefficient n, obtained from Fig. 7(a), versus the NP height (measured by AFM) of the different samples. One can notice that the n values for S1 and S2 are high and at or close to $n = 2$ (3D Debye-like), while n values for S3–S6 are significantly lower, about $n = 1.4$ in average, i.e., between $n = 2$ of the 3D-Debye model and $n = 1$ of the 2D-Debye model. In addition, the value of the coefficient n appears to be independent of the NP height. We will discuss this finding in Sec. IV.

We can define the low-E excess vibrational states (with respect to bulk bcc Fe) as the area below the PDOS, $g(E)$, measured from the lowest experimentally meaningful energy ($E = 2.6$ meV) to a higher, reasonable energy of ~8 meV (in the low-E spectrum) minus the area below $g(E)$ of bulk bcc Fe taken in the same energy interval. This energy interval is similar to that used for the linear fit of the log-log plots in Fig. 7(a). The results are shown in Fig. 8(b), where we plotted the coefficient n versus the excess low-E vibrational states in our samples. Considering only the samples on $SiO_2/Si(111)$ substrates (S2–S6), S2 shows $n = 2.0$ (3D-Debye behavior) and the smallest contribution of excess vibrational states [~38 $(eV)^{-1}$ (at. vol.)$^{-1}$(meV)], while S3–S6 display a larger amount of excess vibrational states and a non-Debye-like $n = 1.4$, which was found to be independent of the relative amount of excess states within error margins. Sample S1, with NPs on an $Al_2O_3(0001)$ substrate, has a nearly Debye-like value of $n = 1.89$ but a higher number of excess vibrational states than S2. This suggests that the type of substrate [$Al_2O_3(0001)$ versus $SiO_2/Si(111)$] has some influence on the PDOS of the NPs.

Figure 8(c) displays the dependence of the excess vibrational states on the NP height for the different samples. An almost linear dependence can be observed for S2, S4, S5, and S6 [NPs on $SiO_2/Si(111)$], with an increase in the excess vibrational density of states with increasing NP height. The same trend can also be observed in Fig. 7(b); only sample S3 deviates from that trend. Because of its different support [$Al_2O_3(001)$], sample S1 is not expected to follow exactly the same trend as S2–S6. For a given substrate, Fig. 8(c) demonstrates an increase in the excess vibrational density of states with increasing NP height. The origin of this effect will be discussed in Sec. IV.

Table II compiles important thermodynamic parameters extracted from the PDOS obtained from RT NRIXS measurements, including the vibrational entropy (S_{vib}), vibrational specific heat (C_{vib}), internal energy (U_{vib}), Helmholtz free energy (F_{vib}), mean phonon energy (E_{av}), mean squared atomic displacement ($\langle x^2 \rangle$), and Debye temperature (θ_D). These parameters were obtained using the expressions given in Refs. 8, 12, and 69. Drastic differences can be observed between several of those quantities for the NP samples with

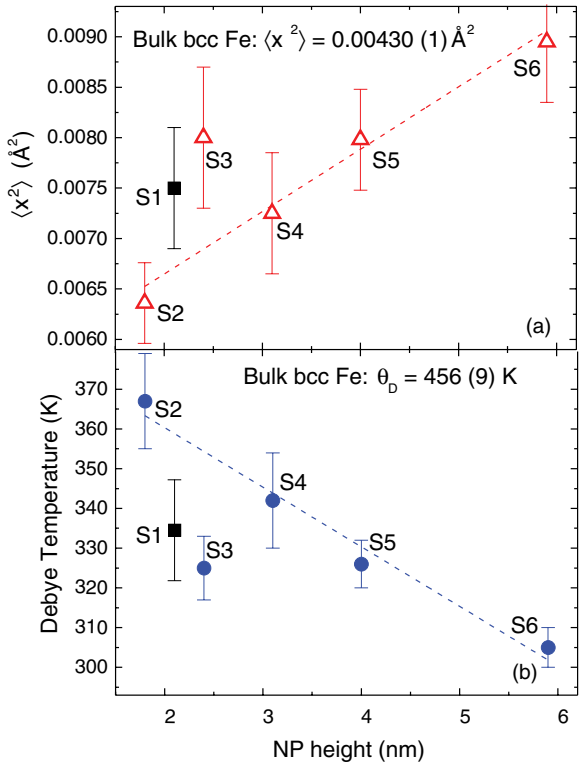

FIG. 9. (Color online) (a) Mean square atomic displacement $\langle x^2 \rangle$ at RT and (b) Debye temperature Θ_D versus NP height (samples S1–S6). The data were deduced from the PDOS shown in Fig. 6(b). (The dashed lines are a guide for the eye.)

respect to bulk bcc Fe. In particular, all NP samples display larger vibrational entropies and specific heats but reduced total internal energies and negative free energies. The largest S_{vib}, C_{vib}, and F_{vib} (negative) values were obtained for the largest NPs (S6). The average mean square atomic displacement at RT is plotted in Fig. 9(a) as a function of the NP height. For a given support [e.g., $SiO_2/SiO_2(111)$, S2–S6], an overall *increase* in $\langle x^2 \rangle$ was observed with increasing NP size, with the largest displacements obtained for the sample containing the largest NPs (S6) and the smallest NPs (S2) being the stiffest [Fig. 9(a)].

Figure 10 displays the calculated thermal evolution of (a) the atomic mean square displacement, (b) the excess vibrational specific heat, and (c) the excess vibrational entropy of the NP samples with respect to bulk bcc Fe. These curves were obtained by inserting the experimental functions $g(E)$ measured at RT into the corresponding integral expressions for the thermodynamic quantities.[8,12,69] Although the error bars of the data in Figs. 10(b) and 10(c) are rather large (representative uncertainties at RT are included in the plot), all NPs (S1–S6) exhibit a significant excess vibrational specific heat and entropy with respect to bulk bcc Fe, whereby our largest NPs (S6) show the most significant differences. Following the Debye model, Θ_D can be obtained from the linear fit of the $\langle x^2 \rangle(T)$ data in Fig. 10(a). The resulting values are shown in Fig. 9(b). Surprisingly, an increase in Θ_D was observed with *decreasing* NP height, with the largest value of 367 K being observed for the ∼1.8 nm NPs in

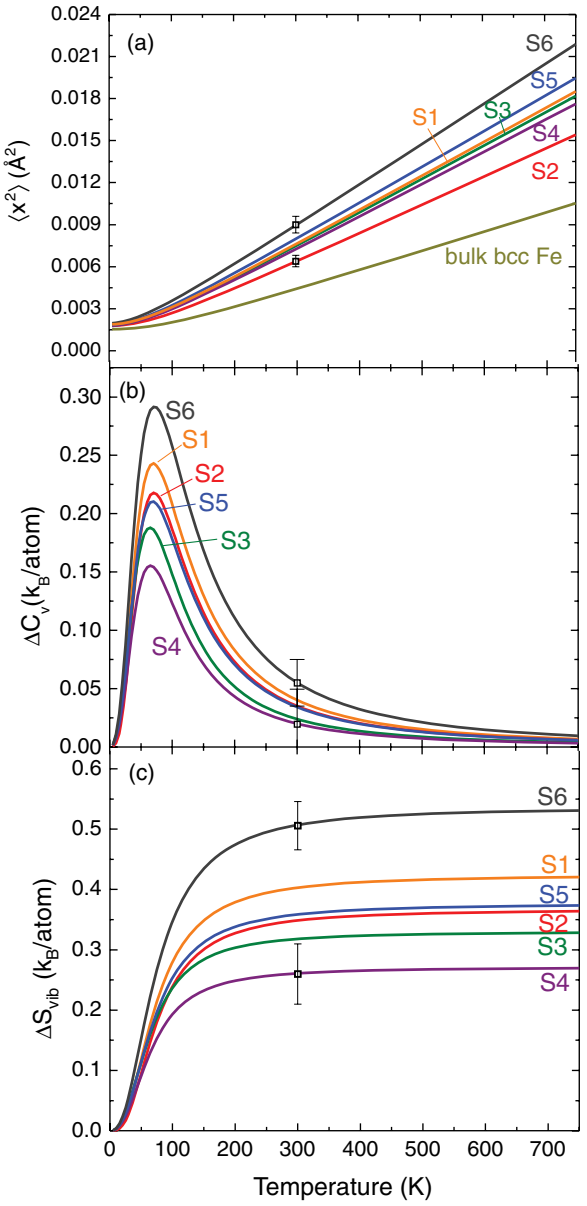

FIG. 10. (Color online) Calculated thermal evolution of the following thermodynamic quantities for samples S1–S6: (a) atomic mean square displacement ($\langle x^2 \rangle$), (b) excess vibrational specific heat (ΔC_{vib}) of the ^{57}Fe NP samples with respect to bulk bcc Fe, and (c) excess vibrational entropy (ΔS_{vib}). The experimental PDOS obtained at RT [shown in Fig. 6(b)] were used in the integral calculation of these quantities.

S2. This behavior is in qualitative agreement with findings for Pt NPs on γ-Al_2O_3 based on extended x-ray absorption fine-structure spectroscopy (EXAFS).[14,15] Nevertheless, all Θ_D values obtained here for the Fe NP samples (306–367 K) were well below that of bulk bcc Fe (456 K), also from NRIXS data. As will be discussed, since drastic deviations from the 3D-Debye model were observed here for the large NPs (S4–S6) at low phonon energy, the Debye temperatures extracted for those systems should be considered as effective Debye temperatures.

TABLE II. The thermodynamic parameters of ^{57}Fe NPs supported on $Al_2O_3(0001)$ (S1) and $SiO_2/Si(111)$ (S2–S6) extracted from the PDOS determined based on NRIXS measurements: vibrational entropy (S_{vib}), vibrational specific heat (C_{vib}), internal vibrational energy (U_{vib}), Helmholtz free energy (F_{vib}), the mean phonon energy (E_{av}), the mean square atomic displacement ($\langle x^2 \rangle$), and the Debye temperature (Θ_D). Data from a bulk Fe reference are also shown. All parameters were obtained at RT.

Sample	S_{vib} (k_B/atom)	C_{vib} (k_B/atom)	U_{vib} (meV/atom)	F_{vib} (meV/atom)	E_{av} (meV/atom)	$\langle x^2 \rangle$ (10^{-2} Å^2)	Θ_D (K)
S1	3.52(6)	2.75(3)	84.0(7)	−7(4)	15.5(8)	0.75(6)	336(11)
S2	3.46(5)	2.75(3)	84.1(7)	−5(4)	16.2(7)	0.64(4)	367(12)
S3	3.43(5)	2.74(2)	84.5(7)	−4(4)	16.3(9)	0.80(7)	325(8)
S4	3.38(6)	2.73(3)	84.6(7)	−2.7(4)	17.0(1)	0.73(6)	342(12)
S5	3.49(3)	2.75(2)	84.2(5)	−5.6(3)	16.3(6)	0.79(5)	326(6)
S6	3.62(4)	2.77(2)	83.6(4)	−10(3)	15.1(6)	0.90(6)	305(5)
Bulk bcc Fe	3.115(5)	2.723(9)	85.05(5)	+4.5(2)	27.30(5)	0.430(1)	456(9)

IV. DISCUSSION

The low-E part of the PDOS ($\sim$3 meV $\leqslant E \leqslant$ 8 meV) was measured with high precision. Here, the main findings for the NPs can be described as follows: (i) an anomalous increase of $g(E)$ (as compared to the PDOS of bulk bcc Fe) with increasing NP height [Fig. 7(a)], i.e., an increase of the excess density of vibrational states [Fig. 8(c)]; (ii) at low E, a deviation from the 3D-Debye behavior for the large NPs (S3–S6), but not for the small NPs (S1, S2), implying a scaling behavior of $g(E) \sim E^n$ [Fig. 7(a)], with the coefficient $n =$ 1.9–2.0 (3D-Debye behavior) for the small NPs (S1, S2) and $n = 1.4$ (non-Debye behavior) for the large NPs (S3–S6) [Fig. 8(a)]; (iii) for the same substrate, the coefficient n versus the excess vibrational states is high ($n = 2$) for the samples with the smallest amount of excess vibrational states (S2) and low ($n = 1.4$) for those with a higher amount of excess vibrational states (S3–S6) [Fig. 8(b)].

Common to these observations is the surprising fact that the anomalous behavior *increases* with increasing NP size. This is contrary to expectation, since usually the anomalous low-E enhancement of the PDOS is attributed in theoretical calculations to low-coordinated weakly bonded surface atoms of free-standing (unsupported) isolated metal NPs,[3,4,7,11,12,44,57] such as Fe NPs on a Ag substrate[51] or Ge NPs.[8] As the surface to volume ratio scales with r^{-1} ($r =$ NP radius), one would expect a reduction of surface effects with increasing NP size. In fact, calculations by Kara and Rahman[55] revealed that the surface-induced enhancement of the low-E PDOS disappeared for NPs with sizes larger than 5 nm. However, the opposite is observed here [Figs. 7(a) and 8(c)]. This observation leads to the conclusion that the measured $g(E)$ enhancement at low E originates from the interior of our Fe NPs and not from their surface. In our experiments, contributions from the interior (core) of the NPs dominate over surface effects with respect to the low-E enhancement of $g(E)$. Two justified assumptions may explain this observation: (1) the suppression of surface effects by the Ti coating, and (2) the formation of a polycrystalline structure in the large Fe NPs, implying grain boundaries in the interior of the NPs with undercoordinated atoms. As to assumption (1), the low-coordinated surface atoms of the NPs are "passivated" by the Ti coating, which results in an increase of their coordination number (more bulk-like) and a reduction of the surface effect on the vibrational properties of the coated NPs at low phonon energies. This explains why the small Fe NPs, which according to TEM are single grain and have no grain boundaries in their interior, behave more like bulk bcc Fe than the larger NPs. One could argue that the Ti coating would create a Ti/Fe interface, which, due to chemical disorder, might also contribute to the low-E phonon enhancement. Although this might be the case to some degree (despite the RT Ti deposition), it cannot be the dominant effect since it should scale with the inverse of the NP size, which, however, is not observed here. The same argument is valid for the phonon contribution of the Fe/support interface, which, for hemispherical NPs on a flat surface, would also scale with the inverse of the NP size. Furthermore, samples S1 and S2 containing small NPs of nearly identical size ($\sim$2 nm), prepared using the same encapsulating polymer and metal/polymer ratio, but deposited on different substrates (SiO_2 versus α-Al_2O_3), display a rather similar PDOS and Debye-like behavior, ruling out the influence of the support as the dominant effect for the anomalies in the PDOS at low E.

Regarding our assumption (2), our TEM images reveal the presence of a multigrain structure in the large NPs [Figs. 3(a)–3(c)], including grain boundaries. The effect of grain boundaries on the PDOS of nanocrystalline materials has been studied extensively experimentally[9,32–42] and theoretically.[7,8,10,13,43–47] In nanocrystalline metals, the low-E enhancement in $g(E)$ was attributed to vibrations of undercoordinated atoms located at interfacial regions of grain boundaries[7,10,40,42,44,46,47] characterized by a softening of force constants.[10] Therefore, we can understand our results if we consider an increase in the fraction of grains and grain boundaries (and related structural defects) within the Fe NPs with increasing NP size, as is qualitatively corroborated by our TEM study (Fig. 3). In particular, assumption (2) explains observation (iii), i.e., the increase in the excess vibrational states with increasing NP height [Fig. 8(c)] in terms of an increase in the fraction of undercoordinated atoms located in the structurally disturbed interfacial regions of grain boundaries (or multiple grain boundaries) in the interior of our Fe NPs. Therefore, the large Fe NPs do not behave like bulk bcc Fe because their internal grain boundaries are not affected by the Ti coating, and atoms at those sites are able to maintain

their low coordination, which results in the observed changes of the vibrational properties.

Also, the observed, different scaling behavior of $g(E) \sim E^n$ [Fig. 7(a)] for the small and large NPs [item (iv)] can be explained in terms of grain-boundary effects. Only our small NPs (S1, S2) closely follow 3D-Debye behavior with $n = 1.9$ (S1) and $n = 2.0$ (S2). We attribute this behavior to the quenching of NP surface effects by the passivating Ti overlayer, which enhances the coordination and increases the force constants of surface atoms. This effect correlates with a low number of excess vibrational states [Figs. 8(b) and 8(c)]. By contrast, the large NPs (S3–S6), which are also passivated by Ti, show $n = 1.4$ (non-Debye behavior) because of the existence of grain boundaries (and possibly other structural defects) in their interior. One should notice that the coefficient n is related to the spatial dimension[47] d via $n = d - 1$. Therefore, the observed value of $n = 1.4$, which lies between $n = 1$ (2D) and $n = 2$ (3D), suggests a reduced effective dimensionality for the low-E Fe atomic vibrations in the grain-boundary regions of the large NPs. The striking observation that $n = 1.4$ is found to be independent of the height of the large NPs [Fig. 8(a)] and also independent of the number of excess vibrational states [Fig. 8(b)] demonstrates that the dimensionality of the grain-boundary phonons at low E and, consequently, the nature of the vibrating Fe species in the grain boundaries, are independent of the NP size.

Our interpretations are corroborated by theoretical calculations of the low-frequency excess modes of the PDOS in bulk nanocrystalline Cu and Ni (model) samples. Derlet *et al.*[46] found a power-law behavior of the low-E grain-boundary PDOS with $n = 1.5$, while $n = 2$ was obtained for $g(E)$ in the interior of the grains. Chadwick[70] calculated the fractal dimension $\bar{d}_{3d}$ of grain boundaries in bulk nanocrystalline Pd and obtained a value of 2.4, in agreement with our dimensionality $d = n + 1 = 2.4$. Also in agreement with our findings is the result of a microscopic lattice dynamical calculation of $g(E)$ in Si nanocrystals, which revealed a low-E behavior intermediate between linear and quadratic.[58] On the other hand, our observation of $n = 1.4$ is at variance with calculations of phonons in polycrystalline Ag NPs by Narvaez *et al.*,[44] which provided $n = 2$ (3D-Debye-like behavior) at low E. Experimentally, Debye-like behavior with $n = 2$ was observed in partially oxidized bulk nanocrystalline Fe ("nanocomposites")[9,38] and attributed to interfacial sites connected to the small crystallite size. Nevertheless, the E^2 behavior in this case might also be due to a fraction of interfacial Fe sites bonded to oxygen atoms, since in our earlier work[51] we have shown that single-grain isolated-supported Fe NPs carrying an Fe-oxide shell are characterized by approximately quadratic behavior, with $n = 1.84$–1.86. However, Stankov *et al.*[42] also obtained E^2 behavior at nanograins and interfaces in bulk nanocrystalline $Fe_{90}Zr_7B_3$ ribbons. Nevertheless, it is conceivable that this discrepancy results from differences in the nature of the grain boundaries (e.g., different width, extension, and structural disorder) in extended bulk nanocrystalline materials and in finite-size nanoscopic grain boundaries in our large NPs. Further studies are required to clarify this question.

The Debye constant α in the relation $g(E) = \alpha E^2$, normalized with the Debye constant α_0 of bulk bcc Fe, is a quantitative measure of the low-E enhancement of $g(E)$. We obtain values of α/α_0 of 3.2 (S1) and 2.2 (S2). Since $\alpha = V/2\pi^2\hbar^3 {v_{\rm av}}^3$ (where V = volume per Fe atom, $\hbar$ = Planck's constant, and $v_{\rm av}$ = average velocity of sound[71]), we can estimate that at RT the average velocity of sound in our small Fe NPs is smaller by a factor of 1.47 (S1) and 1.30 (S2) than $v_{\rm av}$ of bulk bcc Fe. Our α/α_0 values for NPs are of comparable magnitude to those reported by Fultz *et al.*[9] and Stankov *et al.*[42] for bulk nanocrystalline materials containing grain boundaries. We conclude that of some kind of structural disorder must exist also within our smaller NPs, although we have evidence from TEM for the absence of grain boundaries in our small NPs [e.g., in Fig. 4(d) for Fe NPs with a diameter of 4.5 nm, which is twice the AFM NP height for hemispherical NPs]. In this context it is interesting to mention that a disorder–order (amorphous-to-crystalline) transition has been previously reported for Pt NPs on γ-Al_2O_3 above $\sim$1.7 nm,[72] which agrees with our data indicating that the smallest Fe NPs investigated here are already reasonably well ordered. The reduced velocity of sound in samples S1 and S2 with respect to that of bulk bcc Fe is not a surprise even assuming perfect bcc single crystals. One has to keep in mind that in hemispherical particles, e.g., with 2-nm NP height, up to about 49% vol. of the Fe atoms are located at the particle surface, i.e., forming Ti/Fe and Fe/SiO_2 interfaces. Therefore, they exhibit disturbed coordination compared to that of atoms located in the particles core, which most likely leads to the observed softening of the PDOS.

The measured anomalies in $g(E)$ lead to excess specific heat, $\Delta C_{\rm vib}$, and excess vibrational entropy, $\Delta S_{\rm vib}$, in Fe NPs [Figs. 10(b) and 10(c)]. Interestingly, calculations by Kara *et al.*[10] revealed a decrease in $\Delta S_{\rm vib}$ for single grain Ag NPs with increasing NP size from 2.5 to 3.5 nm. However, the opposite trend is observed in Fig. 10(c). In spite of the large uncertainty of the data at high temperature, $\Delta S_{\rm vib}$ for the largest polycrystalline NPs (S6) is significantly higher than that of the smaller polycrystalline NPs (S3–S5) and of the small single grain NPs (S1, S2). (The error bars in $\Delta S_{\rm vib}$ are too large for samples S1–S5 to observe any significant systematics.) This surprising behavior was theoretically predicted by Kara *et al.*,[10] who showed for polycrystalline Ag NPs that atoms in grain boundaries contribute to the low-E and high-E end of $g(E)$. This remarkably enhances $\Delta S_{\rm vib}$ of polycrystalline Ag NPs with respect to single grain Ag NPs of similar size and stabilizes polycrystalline Ag NPs of 4 nm in size by as much as 0.1 k_B/atom at RT.[4] Singh and Prakash[43] calculated $\Delta S_{\rm vib} \approx 0.033\ k_B$/atom at 300 K for single grain Ni nanocrystals. Fultz *et al.*[9] reported a very small value of only $\Delta S_{\rm vib} = 0.01 \pm 0.02\ k_B$/atom for nanocrystalline Fe (nanocomposites) at 300 K. However, other nanocrystalline materials (nanocomposites) showed $\Delta S_{\rm vib}$ values of up to 0.2 k_B/atom.[32,34,35] Our largest polycrystalline NPs (S6) have a value of $\Delta S_{\rm vib} = 0.50 \pm 0.05\ k_B$/atom at 300 K, surpassing all $\Delta S_{\rm vib}$ of our smaller (single grain or polycrystalline) Fe NPs and all aforementioned literature values. The thermodynamic stability of our large Fe NPs (S6) should be strongly affected by such a large value of the excess vibrational entropy.

The largest excess vibrational specific heat $\Delta C_{\rm vib}$ in our NPs was found for our largest (polycrystalline) Fe NPs (S6) [Fig. 10(b)]. We observe $\Delta C_{\rm vib} = 0.05 \pm 0.03\ k_B$/atom at

300 K and ∼0.275 k_B/atom in the maximum at $T \approx 70$ K. This corresponds to enhancements of ∼1.8% at 300 K and ∼35% at 70 K [relative to $C_{vib} = 2.72$ k_B/atom at 300 K (Table II) and ∼0.78 k_B/atom at 70 K for bulk bcc Fe[5]] for Fe NPs in S6. For Fe NPs in S4 the relative enhancements are ∼0.4% at 300 K and ∼18% at 70 K. Large excess specific heat ΔC_{vib} was also observed experimentally for nanocrystalline (nanocomposite) Fe[5] and Pt,[73,74] although the influence of light-element impurity atoms plays a role there.[74] In the case of our Fe NPs, impurity atoms were not detected by XPS analysis; thus, impurities are not responsible for the thermodynamic modifications of $g(E)$ and the excess specific heat obtained. The low temperature maximum of $\Delta C_{vib}(T)$ in nanoscale systems was also observed in theoretical calculations.[7,8,13,58] It originates from the enhanced PDOS at low phonon energies. For nanocrystalline (model) samples, the low-T maximum in $\Delta C_{vib}(T)$ was calculated to be near 50 K for Cu[7] and near 90–100 K for Ge[8] and Si[58] and nearly independent of the nanograin size. The latter result is in agreement with our finding for Fe NPs [Fig. 10(b)]. The theoretically calculated maximum enhancements at low T for nanocrystalline (model) materials amount to ∼11% for Cu[7] and ∼8–15% for Si,[58] the latter value decreasing with increasing Si nanograin size (2.1–3.3 nm).[58] These theoretical enhancements are of the same order of magnitude as those observed for our Fe NPs at low T.

The derived values for the excess vibrational entropy and lattice specific heat of sample S6 are unusually high in comparison to the published data. They exceed even the values derived for fully disordered Fe by Stankov *et al.*[50] and might not be explained solely by the presence of grain boundaries with nonperfect bcc structure. This applies not only to sample S6 but also to the rest of the samples studied (Table II). This difference might be an indication of the influence of the Fe/Ti and Fe/SiO_2 interfaces or of additional unknown defects (other than grain boundaries) on the vibrational thermodynamics of the investigated NPs.

V. CONCLUSIONS

Our experimental investigation demonstrates that, in combination with structural information obtained via TEM, NRIXS measurements can be used to extract information on the degree of internal structural disorder of metal NPs due to the strong correlation between the internal structure of the NPs and the low- and high-E vibrational spectra. In particular, large Fe particles (>2 nm) with an enhanced content of grain boundaries and structural defects were found to display excess PDOS at low-E, excess vibrational specific heat and excess vibrational entropy with respect to bulk bcc Fe. In addition, a size-dependent trend was observed for the atomic mean square displacement ($\langle x^2 \rangle$) and the Debye temperature (Θ_D) extracted from room-temperature NRIXS measurements, with the smallest $\langle x^2 \rangle$ values and highest Θ_D values obtained for the smallest NPs investigated (∼1.8 nm). Furthermore, although overall smaller Debye temperatures than those of bulk bcc Fe were obtained for all NP sizes, an increase in the Debye temperature was observed with decreasing NP size. The opposite trend was observed for the atomic displacements used to extract the Debye temperatures, namely, a decrease in $\langle x^2 \rangle$ with decreasing NP size. It is concluded that the larger NPs are softer due to the existence of grain boundaries in their interior. Also the observed different scaling behavior of $g(E) \sim E^n$ may be explained by assuming a polycrystalline structure for large NPs (>2 nm) and a single grain structure for the small NPs (⩽2 nm). The coefficient $n = 1.4$ for the large NPs suggests a reduced effective dimensionality of 2.4 due to the low-E vibrational modes at grain boundaries. The thermodynamic quantities of our supported isolated Fe NPs show distinct anomalies in qualitative agreement with those of theoretical calculations reported in the literature.

ACKNOWLEDGMENTS

W.K. appreciates stimulating discussions with J. Kirschner and M. Przybylski (both Halle), G. Bayreuther (Halle and Regensburg), and M. E. Gruner and P. Entel (both Duisburg-Essen). Financial support from the US National Science Foundation (DMR-0906562) is greatly appreciated. Use of the Advanced Photon Source facilities at Argonne National Laboratory and that of the electron microscopy facilities at the Center for Functional Nanomaterials at Brookhaven National Laboratory were supported by the US Department of Energy under Contracts DEAC02-06CH11357 and DE-AC02-98CH10886, respectively. The research at the University of New Mexico was supported by the DOE-EERE Office of Fuel Cell Technology.

*Corresponding author: roldan@ucf.edu

[1] M. A. Stroscio and M. Dutta, eds., *Phonons in Nanostructures* (Cambridge University Press, Cambridge, England, 2001).
[2] B. Fultz, Prog. Mater. Sci. **55**, 247 (2010).
[3] D. Y. Sun, X. G. Gong, and X. Q. Wang, Phys. Rev. B **63**, 193412 (2001).
[4] A. Kara and T. S. Rahman, Surf. Sci. Rep. **56**, 159 (2005).
[5] Y. H. Bai, J. L. Luo, D. Jin, and J. R. Sun, J. Appl. Phys. **79**, 361 (1996).
[6] Z.-C. Tan, L. Wang, and Q. Shi, Pure Appl. Chem. **81**, 1871 (2009).
[7] R. Meyer, L. J. Lewis, S. Prakash, and P. Entel, Phys. Rev. B **68**, 104303 (2003).
[8] D. Sopu, J. Kotakoski, and K. Albe, Phys. Rev. B **83**, 245416 (2011).
[9] B. Fultz, C. C. Ahn, E. E. Alp, W. Sturhahn, and T. S. Toellner, Phys. Rev. Lett. **79**, 937 (1997).
[10] A. Kara, A. N. Al-Rawi, and T. Rahman, J. Comput. Theor. Nanosci. **1**, 216 (2004).
[11] S. R. Calvo and P. B. Balbuena, Surf. Sci. **581**, 213 (2005).
[12] H. Yildirim, A. Kara, and T. S. Rahman, J. Phys.: Condens. Matter. **21**, 084220 (2009).
[13] R. Singh, S. Prakash, R. Meyer, and P. Entel, PRAMANA- J. Phys. (Indian Acad. Sci.) **60**, 547 (2003).
[14] B. Roldan Cuenya, M. Alcántara Ortigoza, L. K. Ono, F. Behafarid, S. Mostafa, J. R. Croy, K. Paredis, G. Shafai, T. S. Rahman, L. Li, Z. Zhang, and J. C. Yang, Phys. Rev. B **84**, 245438 (2011).

[15]B. Roldan Cuenya, A. I. Frenkel, S. Mostafa, F. Behafarid, J. R. Croy, L. K. Ono, and Q. Wang, Phys. Rev. B **82**, 155450 (2010).
[16]G. D. Barrera, J. A. O. Bruno, T. H. K. Barron, and N. L. Allen, J. Phys.: Condens. Matter **17**, R217 (2005).
[17]F. D. Vila, J. J. Rehr, J. Kas, R. G. Nuzzo, and A. I. Frenkel, Phys. Rev. B **78**, 121404 (2008).
[18]Q. S. Mei and K. Lu, Progr. Mater. Sci. **52**, 1175 (2007).
[19]R. M. Costescu, D. G. Cahill, F. H. Fabreguette, Z. A. Sechrist, and S. M. George, Science **303**, 989 (2004).
[20]D. G. Cahill, W. K. Ford, K. E. Goodson, G. D. Mahan, A. Majumdar, H. J. Maris, R. Merlin, and S. R. Phillpot, Appl. Phys. Rev. **93**, 793 (2003).
[21]G. J. Snyder and E. S. Toberer, Nat. Mater. **7**, 105 (2008).
[22]I. Ponomareva, D. Srivastava, and M. Menon, Nano Lett. **7**, 1155 (2007).
[23]G. M. Veith, A. R. Lupini, S. Rashkeev, S. J. Pennycook, D. R. Mullins, V. Schwartz, C. A. Bridges, and N. J. Dudney, J. Catal. **262**, 92 (2009).
[24]G. Baffou, R. Quidant, and C. Girard, Phys. Rev. B **82**, 165424 (2010).
[25]D. Vashaee and A. Shakouri, Phys. Rev. Lett. **92**, 106103 (2004).
[26]J. Yang, J. You, C.-C. Chen, W.-C. Hsu, H. Tan, X. Wang Zhang, Z. Hong, and Y. Yang, ACS Nano **5**, 6210 (2011).
[27]W. Fei, A. Kara, and T. S. Rahman, Phys. Rev. B **61**, 16105 (2000).
[28]N. Wiele, H. Franz, and W. Petry, Physica B **263**, 716 (1999).
[29]M. Matsui, H. Yamada, and K. Adachi, J. Phys. Soc. Jpn. **48**, 2161 (1980).
[30]H. Yildirim, A. Kara, S. Durukanoglu, and T. S. Rahman, Surf. Sci. **600**, 484 (2006).
[31]B. Gumhalter and T. Matsushima, Surf. Sci. **561**, 183 (2004).
[32]B. Fultz, L. Anthony, L. J. Nagel, R. M. Nicklow, and S. Spooner, Phys. Rev. B **52**, 3315 (1995).
[33]J. Trampenau, K. Bauszus, W. Petry, and U. Herr, Nanostruct. Mater. **6**, 551 (1995).
[34]B. Fultz, J. L. Robertson, T. Stephens, L. Nagel, and S. Spooner, J. Appl. Phys. **79**, 8318 (1996).
[35]H. N. Frase, L. J. Nagel, J. L. Robertson, and B. Fultz, Philos. Mag. B **75**, 335 (1997).
[36]H. Frase, B. Fultz, and J. L. Robertson, Phys. Rev. B **57**, 898 (1998).
[37]U. Stuhr, H. Wipf, K. H. Andersen, and H. Hahn, Phys. Rev. Lett. **81**, 1449 (1998).
[38]L. Pasquini, A. Barla, A. I. Chumakov, O. Leupold, R. Ruffer, A. Deriu, and E. Bonetti, Phys. Rev. B **66**, 073410 (2002).
[39]E. Bonetti, L. Pasquini, E. Sampaolesi, A. Deriu, and G. Cicognani, J. Appl. Phys. **88**, 4571 (2000).
[40]A. B. Papandrew, A. F. Yue, B. Fultz, I. Halevy, W. Sturhahn, T. S. Toellner, E. E. Alp, and H. K. Mao, Phys. Rev. B **69**, 144301 (2004).
[41]A. F. Yue, A. B. Papandrew, O. Delaire, B. Fultz, Z. Chowdhuri, R. M. Dimeo, and D. A. Neumann, Phys. Rev. Lett. **93**, 205501 (2004).
[42]S. Stankov, Y. Z. Yue, M. Miglierini, B. Sepiol, I. Sergueev, A. I. Chumakov, L. Hu, P. Svec, and R. Rüffer, Phys. Rev. Lett. **100**, 235503 (2008).
[43]R. Singh and S. Prakash, Surf. Sci. **532–535**, 272 (2003).
[44]G. A. Narvaez, J. Kim, and J. W. Wilkins, Phys. Rev. B **72**, 155411 (2005).
[45]P. M. Derlet and H. V. Swygenhoven, Phys. Rev. Lett. **92**, 035505 (2004).
[46]P. M. Derlet, R. Meyer, L. J. Lewis, U. Stuhr, and H. Van Swygenhoven, Phys. Rev. Lett. **87**, 205501 (2001).
[47]C. Hudon, R. Meyer, and L. J. Lewis, Phys. Rev. B **76**, 045409 (2007).
[48]H. Gleiter, Prog. Mater. Sci. **33**, 223 (1989).
[49]R. W. Siegel, Phys. Today **46**, 64 (1993).
[50]S. Stankov, M. Miglierini, A. I. Chumakov, I. Sergueev, Y. Z. Yue, B. Sepiol, P. Svec, L. Hu, and R. Rüffer, Phys. Rev. B **82**, 144301 (2010).
[51]B. Roldan Cuenya, A. Naitabdi, J. Croy, W. Sturhahn, J. Y. Zhao, E. E. Alp, R. Meyer, D. Sudfeld, E. Schuster, and W. Keune, Phys. Rev. B **76**, 195422 (2007).
[52]B. Roldan Cuenya, J. R. Croy, L. K. Ono, A. Naitabdi, H. Heinrich, W. Keune, J. Zhao, W. Sturhahn, E. E. Alp, and M. Hu, Phys. Rev. B **80**, 125412 (2009).
[53]B. Roldan Cuenya, L. K. Ono, J. R. Croy, A. Naitabdi, H. Heinrich, J. Zhao, E. E. Alp, W. Sturhahn, and W. Keune, Appl. Phys. Lett. **95**, 143103 (2009).
[54]R. Meyer, S. Prakash, and P. Entel, Phase Transitions **75**, 51 (2002).
[55]A. Kara and T. S. Rahman, Phys. Rev. Lett. **81**, 1453 (1998).
[56]R. Meyer and P. Entel, Z. Kristallogr. **222**, 646 (2007).
[57]S. Durukanoglu, A. Kara, and T. S. Rahman, Phys. Rev. B **67**, 235405 (2003).
[58]X. Hu, G. Wang, W. Wu, P. Jiang, and J. Zi, J. Phys.: Condens. Matter **13**, L835 (2001).
[59]B. Roldan Cuenya, J. R. Croy, S. Mostafa, F. Behafarid, L. Li, Z. F. Zhang, J. C. Yang, Q. Wang, and A. I. Frenkel, J. Am. Chem. Soc. **132**, 8747 (2010).
[60]See Supplemental Material at http://link.aps.org/supplemental/10.1103/PhysRevB.86.165406 for additional information on the nanoparticle height and interparticle distance histograms (AFM) as well as additional chemical characterization of all as-prepared samples via XPS.
[61]W. Sturhahn, Hyperfine Interact. **125**, 149 (2000).
[62]S.-C. Y. Tsen, P. A. Crozier, and J. Liu, Ultramicroscopy **98**, 63 (2003).
[63]J.-O. Malm and M. A. O'Keefe, Ultramicroscopy **68**, 13 (1997).
[64]NIST X-ray Photoelectron Spectroscopy Database, (Version 3.4), http://srdata.nist.gov/xps/index.htm (2011).
[65]A. I. Chumakov, R. Rüffer, H. Grünsteudel, H. F. Grünsteudel, G. Grubel, J. Metge, and H. A. Goodwin, Europhys. Lett. **30**, 427 (1995).
[66]M. Seto, Y. Yoda, S. Kikuta, X. W. Zhang, and M. Ando, Phys. Rev. Lett. **74**, 3828 (1995).
[67]W. Sturhahn, T. S. Toellner, E. E. Alp, X. Zhang, M. Ando, Y. Yoda, S. Kikuta, M. Seto, C. W. Kimball, and B. Dabrowski, Phys. Rev. Lett. **74**, 3832 (1995).
[68]B. Roldan Cuenya, W. Keune, R. Peters, E. Schuster, B. Sahoo, U. von Hörsten, W. Sturhahn, J. Zhao, T. S. Toellner, E. E. Alp, and S. D. Bader, Phys. Rev. B **77**, 165410 (2008).
[69]E. E. Alp, W. Sturhahn, T. S. Toellner, J. Zhao, M. Mu, and D. E. Brown, Hyperfine Interact. **144/145**, 3 (2002).
[70]J. Chadwick, J. Phys.: Condens. Matter **11**, 129 (1999).
[71]R. Lübbers, H. F. Grünsteudel, A. I. Chumakov, and G. Wortmann, Science **287**, 1250 (2000).
[72]L. Li, L.-L. Wang, S. I. Sanchez, J. H. Kang, Q. Wang, Z. Zhang, A. I. Frenkel, D. D. Johnson, R. G. Nuzzo, and J. C. Yang, Microscopy and Microanalysis **15**, 1210 (2009).
[73]J. Rupp and R. Birringer, Phys. Rev. B **36**, 7888 (1987).
[74]A. Tschöpe and R. Birringer, Philos. Mag. B **68**, 223 (1993).